Simultaneously Coupled Mechanical-Electrochemical-Thermal Simulation of Lithium-Ion Cells

Preprint

Chao Zhang, Shriram Santhanagopalan, Michael A. Sprague, and Ahmad A. Pesaran

Presented at the 229th Meeting of the Electrochemical Society (ECS 229)
San Diego, California
May 29 – June 2, 2016

NREL is a national laboratory of the U.S. Department of Energy
Office of Energy Efficiency & Renewable Energy
Operated by the Alliance for Sustainable Energy, LLC

This report is available at no cost from the National Renewable Energy Laboratory (NREL) at www.nrel.gov/publications.

Conference Paper
NREL/CP-5400-66962
August 2016

Contract No. DE-AC36-08GO28308

NOTICE

This report is available at no cost from the National Renewable Energy Laboratory (NREL) at www.nrel.gov/publications.

Available electronically at SciTech Connect http:/www.osti.gov/scitech

Available for a processing fee to U.S. Department of Energy and its contractors, in paper, from:

U.S. Department of Energy
Office of Scientific and Technical Information
P.O. Box 62
Oak Ridge, TN 37831-0062
OSTI http://www.osti.gov
Phone: 865.576.8401
Fax: 865.576.5728
Email: reports@osti.gov

Available for sale to the public, in paper, from:

U.S. Department of Commerce
National Technical Information Service
5301 Shawnee Road
Alexandria, VA 22312
NTIS http://www.ntis.gov
Phone: 800.553.6847 or 703.605.6000
Fax: 703.605.6900
Email: orders@ntis.gov

Cover Photos by Dennis Schroeder: (left to right) NREL 26173, NREL 18302, NREL 19758, NREL 29642, NREL 19795.

NREL prints on paper that contains recycled content.

Simultaneously Coupled Mechanical-Electrochemical-Thermal Simulation of Lithium-Ion Cells

C. Zhang[a], S. Santhanagopalan[b], M. A. Sprague[a], A. A. Pesaran[b]

[a] Computational Science Center, National Renewable Energy Laboratory, Golden, Colorado 80401, USA
[b] Transportation and Hydrogen Systems Center, National Renewable Energy Laboratory, Golden, Colorado 80401, USA

Understanding the combined electrochemical-thermal and mechanical response of a system has a variety of applications, for example, structural failure from electrochemical fatigue and the potential induced changes of material properties. For lithium-ion batteries, there is an added concern over the safety of the system in the event of mechanical failure of the cell components. In this work, we present a generic multi-scale simultaneously coupled mechanical-electrochemical-thermal model to examine the interaction between mechanical failure and electrochemical-thermal responses. We treat the battery cell as a homogeneous material while locally we explicitly solve for the mechanical response of individual components using a homogenization model and the electrochemical-thermal responses using an electrochemical model for the battery. A benchmark problem is established to demonstrate the proposed modeling framework. The model shows the capability to capture the gradual evolution of cell electrochemical-thermal responses, and predicts the variation of those responses under different short-circuit conditions.

Introduction

The safety behavior of lithium-ion battery structures under an external mechanical crush is a critical concern for its application in electrical vehicles. There is a significant increase in efforts on the mechanical performance and safety modeling of battery cells during the last few years (1–18). Wierzbicki and Sahraei et al. conducted a series of experimental and numerical studies to understand effective mechanical properties and failure of battery cells and cell components (separator and electrodes) (1–5). Lai and Ali et al. studied the mechanical properties of batteries on representative volume element (RVE) specimens of prismatic graphite/$LiFePO_4$ pouch cells and developed corresponding computational models (6–9). Xu et al. studied extensively the strain rate dependent and state-of-charge (SOC) dependent mechanical properties of cylindrical 18650 cells (10–13). Pannala (14) and Wang (15) presented experimental studies of internal damage and proposed a Virtual Integrated Battery Environment (VIBE) for modeling of batteries (14, 15). Recently, we presented the first coupled mechanical-electrical-thermal model for simulating mechanical abuse-induced short circuits and identified the interaction of mechanical failure and consequential electrical-thermal response. For example, an increase of 0.06 mm in the indenter displacement followed by a short circuit results in a 20 fold increase of current flowing between the electrodes (16, 17). These findings further drive the need for developing modeling tools for accurate prediction of internal failure behavior and short-circuit location. The cell-level models

presented in the literature were either a macro-scale homogenized model (1–5) or used a simplified model with reduced number of layers (16, 17).

In this work, we present a multi-scale simultaneously coupled mechanical-electrochemical-thermal model built using a commercial finite element software LS-DYNA. This model is computationally efficient, and enables an accurate prediction of the electrochemical-thermal response during an evolving mechanical failure accompanied by internal short circuit. Detailed description of the approach is presented in the next section, followed by a benchmark study using a single element. A summary and scope for future work are presented in the conclusion section.

Approach and Theory

The objective of this work is to enable a simultaneous modeling of electrochemical reactions during a mechanical abuse induced short. The proposed model is capable of studying the interactions between mechanical failure and battery cell performance, through incorporation of temperature evolution from multiple sources (mechanical heat, Joule heat and electrochemical heat) and determination of the short resistance from the results of the mechanical failure simulation as a function of time. Using a multi-scale approach, the model predicts the actual location of failure initiation during a mechanical crush test, while maintaining an acceptable computational efficiency. The modeling approach involves the following aspects:

Simultaneous Multi-scale Modeling Framework

Figure 1 shows the finite element mesh of the cell indentation model and the scheme for the multi-scale simultaneously coupled model. At the macro-scale, the model is homogeneous with a uniform element size as shown in the finite element mesh. Each macro element represents a representative volume element of the battery cell, which is a stacking of anode, separator, and cathode. A volume-average based homogenization model is introduced to analyze the actual deformation and failure of each component. On the other hand, the mechanical model is coupled with an electrochemical-thermal model in micro-scale to transfer failure status of the separator layer, to predict the electrical short circuit resistance and to simulate the consequential electrical/thermal responses (current increase and drop, voltage drop and thermal runaway). The temperature within each element at the macro-scale thermal model is considered uniform, but the thermal sources coming from the electrochemical–thermal model vary from one element to another. The model presented is implemented in the commercial finite element software LS-DYNA through a user-defined material model. In the sections below, we present a simple introduction to each of the models, and the coupling method.

Mechanical Homogenization Model

A general homogenization methodology is introduced to obtain the effective properties of the element for the macro-scale model and solve the stress/strain responses of individual components. As a preliminary study, we consider an anisotropic, linear elastic and rectangular plate. A Cartesian coordinate system (x,y,z) is attached to the plate in such a way that the origin is at one of the four corners on the top surface and the plate is in the positive z-region. The linear constitutive equations of a homogeneous elastic material can be written as

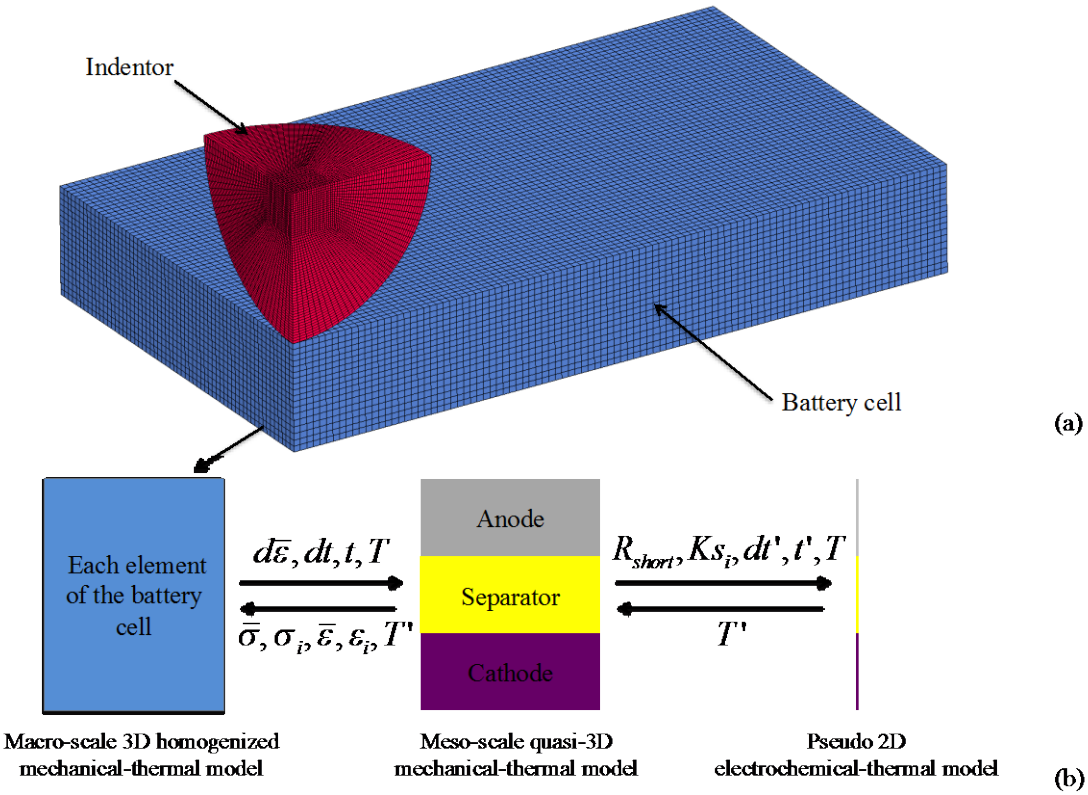

Figure 1. Scheme of the multi-scale simultaneously coupled mechanical-electrochemical-thermal modeling framework for mechanical abuse of lithium-ion battery.

$$\sigma_{ij} = C_{ijkl}\varepsilon_{kl} \tag{1}$$

where σ_{ij} and ε_{kl} are the stress and strain components, C_{ijkl} the elastic stiffness matrix. The stress/strain components can be partitioned into in-plane and out-plane vectors (corresponding to the subscripts $\parallel$ and $\perp$ respectively). For example, the stress components are organized as follows:

$$\boldsymbol{\sigma}_{\perp} = \{\sigma_{33}, \sigma_{23}, \sigma_{13}\}^T \quad \boldsymbol{\sigma}_{\parallel} = \{\sigma_{11}, \sigma_{22}, \sigma_{12}\}^T \tag{2}$$

In Eq. [2], the superscript T denotes the matrix transpose. Subscripts 1, 2 and 3 indicate the in-plane x, y and the out-of-plane z directions, respectively. Then, the constitutive equation [1] can be equivalently written in the following concise matrix form:

$$\boldsymbol{\sigma}_{\parallel} = \boldsymbol{C}_{\parallel}\boldsymbol{\varepsilon}_{\parallel} + \boldsymbol{C}_{\times}^{T}\boldsymbol{\varepsilon}_{\perp} \tag{3}$$

$$\boldsymbol{\sigma}_{\perp} = \boldsymbol{C}_{\times}\boldsymbol{\varepsilon}_{\parallel} + \boldsymbol{C}_{\perp}\boldsymbol{\varepsilon}_{\perp} \tag{4}$$

where $\boldsymbol{C}_{\perp}$, $\boldsymbol{C}_{\parallel}$, $\boldsymbol{C}_{\times}$ and $\boldsymbol{C}_{\times}^{T}$ are the generalized Voigt matrices given by:

$$\boldsymbol{C}_{\parallel} = \begin{bmatrix} C_{11} & C_{12} & C_{16} \\ C_{12} & C_{22} & C_{26} \\ C_{16} & C_{26} & C_{66} \end{bmatrix} \quad \boldsymbol{C}_{\perp} = \begin{bmatrix} C_{33} & C_{34} & C_{35} \\ C_{34} & C_{44} & C_{45} \\ C_{35} & C_{45} & C_{55} \end{bmatrix} \quad \boldsymbol{C}_{\times} = \begin{bmatrix} C_{13} & C_{23} & C_{36} \\ C_{14} & C_{24} & C_{46} \\ C_{15} & C_{25} & C_{56} \end{bmatrix} \tag{5}$$

Next, we consider a composite plate consisting of N layers with each being homogeneous material as shown in Figure 2. In the following description, we use a

superscript (i) to the quantities associated with each layer i (i=1,2,…,N). We assume that the displacements and tractions are continuous across each interface, and that the total thickness of the plate (H) is much lower than the in-plane dimensions (L_x, L_y). Then the in-plane strain in each layer is the same, and equal to the effective strain:

$$\bar{\boldsymbol{\varepsilon}}_{\parallel} = \boldsymbol{\varepsilon}_{\parallel}^{(1)} = \boldsymbol{\varepsilon}_{\parallel}^{(2)} = \cdots = \boldsymbol{\varepsilon}_{\parallel}^{(N)} \tag{6}$$

where the over bar represents effective properties of the layered composite. The effective out-of-plane strain is taken to be the volume (thickness) average of the strain in layers:

$$\bar{\boldsymbol{\varepsilon}}_{\perp} = v^{(1)}\boldsymbol{\varepsilon}_{\perp}^{(1)} + v^{(2)}\boldsymbol{\varepsilon}_{\perp}^{(2)} + \cdots + v^{(N)}\boldsymbol{\varepsilon}_{\perp}^{(N)} \tag{7}$$

where $v^{(i)} = h^{(i)}/H$ is the volume fraction of the i-th layer and $H = h^{(1)} + h^{(2)} + \cdots + h^{(N)}$ is the total height. The volume averaged in-plane stress ($\bar{\boldsymbol{\sigma}}_{\parallel}$) is related to the stress in the individual layers ($\boldsymbol{\sigma}_{\parallel}^{(i)}$) as follows:

$$\bar{\boldsymbol{\sigma}}_{\parallel} = v^{(1)}\boldsymbol{\sigma}_{\parallel}^{(1)} + v^{(2)}\boldsymbol{\sigma}_{\parallel}^{(2)} + \cdots + v^{(N)}\boldsymbol{\sigma}_{\parallel}^{(N)} \tag{8}$$

and the out-of-plane stress in each layer is the same and equal to the effective out-of-plane stress:

$$\bar{\boldsymbol{\sigma}}_{\perp} = \boldsymbol{\sigma}_{\perp}^{(1)} = \boldsymbol{\sigma}_{\perp}^{(2)} = \cdots = \boldsymbol{\sigma}_{\perp}^{(N)} \tag{9}$$

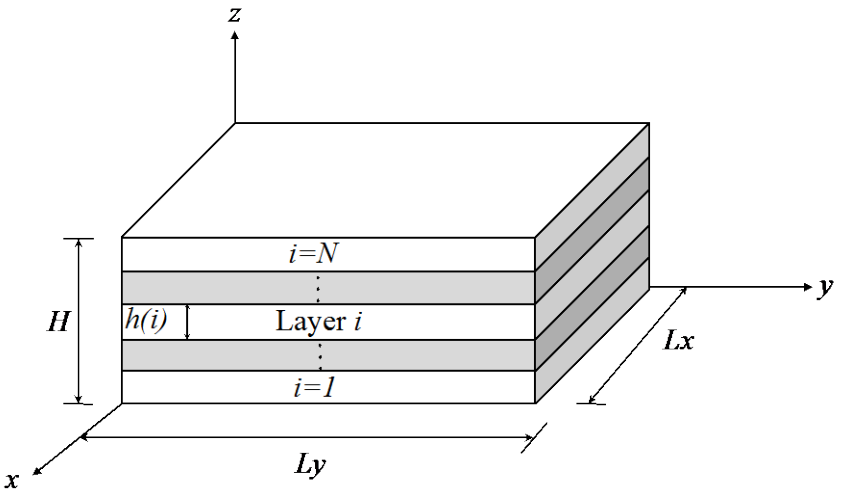

Figure 2. Schematic of the representative sandwich in a multi-layer representation of the cell: the z-dimension (through thickness) is usually orders of magnitude smaller compared to the in-plane (x and y) dimensions in a cell.

Substituting the constitutive equations above and following the procedure outlined in (18), we can then solve explicitly for components of the effective stiffness as follows:

$$\bar{\boldsymbol{C}}_{\perp} = \left[\sum_{i=1}^{N} v^{(i)}\left(\boldsymbol{C}_{\perp}^{(i)}\right)^{-1}\right]^{-1} \tag{10}$$

$$\overline{\boldsymbol{C}}_{\times} = \overline{\boldsymbol{C}}_{\perp}\left[\sum_{i=1}^{N} v^{(i)}\left(\boldsymbol{C}_{\perp}^{(i)}\right)^{-1}\boldsymbol{C}_{\times}^{(i)}\right] \tag{11}$$

$$\overline{\boldsymbol{C}}_{\times}^{T} = \left[\sum_{i=1}^{N} v^{(i)}\boldsymbol{C}_{\times}^{(i)^{T}}\left(\boldsymbol{C}_{\perp}^{(i)}\right)^{-1}\right]\overline{\boldsymbol{C}}_{\perp} \tag{12}$$

$$\overline{\boldsymbol{C}}_{\parallel} = \sum_{i=1}^{N} v^{(i)}\boldsymbol{C}_{\parallel} + \sum_{i=1}^{N} v^{(i)}\boldsymbol{C}_{\times}^{(i)^{T}}\left(\boldsymbol{C}_{\perp}^{(i)}\right)^{-1}\left(\overline{\boldsymbol{C}}_{\times} - \boldsymbol{C}_{\times}^{(i)}\right) \tag{13}$$

So far, we have derived the effective stiffness components for the macro-scale homogenized element. For an explicit simulation, an incremental strain tensor should be calculated based on the loading and boundary conditions, with which we will then be able to calculate the effective stress and effective strain histories. Implementing the effective stress and strain, and the constitutive equations [1]–[5] into the governing equations [6]–[9], we can then calculate the stress and strain histories for each individual layer. The deformation histories for the components can be coupled with the electrical-thermal properties, for example, evolution of conductivity and porosity with layer thickness/volume. On the other hand, we can predict the continuous change in the short-resistance using specific failure criteria defined for each component based on their mechanical responses. This homogenization approach can be extended to a nonlinear material by including plastic components into the constitutive equation [1]. The assumptions related to equations [6]–[9] are still applicable.

Electrochemical-Thermal Model

For illustrative purposes, we used a simple electrochemical model described by Guo and White (22). The cell voltage as a function of lithium ion concentration within the individual electrodes ($x_{Li,j}$) was modified to the following equations:

$$V_{Cell} = U_p - U_n + \sum_{j=n,p} \frac{2RT}{F} ln\left(\frac{\sqrt{m_j^2 + 4} + m_j}{2}\right) - i_{app}R_{Short} \tag{14}$$

$$\text{where} \qquad m_j = \frac{i_{app}}{Fk_jS_jc_{s,j}^{max}c_e^{0.5}\left(1 - x_{Li,j}\right)^{0.5}x_{Li,j}^{0.5}} \tag{15}$$

The evolution of temperature with the drop in cell voltage is given by:

$$\rho\upsilon c_p\frac{\partial T}{\partial t} = i_{app}\left\{V_{Cell} - \left(U_p - U_n\right) + i_{app}R_{Short}\right\} - q \tag{16}$$

In equation [16], the contributions from entropy change with temperature have been neglected. The last term q represents heat transfer to the surroundings. In the set of results discussed in this work, this term was set equal to zero, corresponding to an adiabatic test condition. A complete description of the parameters and derivation of the expressions is presented in (22). Additional description of the parameter R_{short}, the short circuit resistance is provided in the following section.

Mechanical-Electrochemical-Thermal Coupling

Extensive studies have been conducted in the literature examining the interaction between mechanical stress/strain and electrochemical-thermal reactions (19, 20). For example, Golmon et al. (20) developed a multi-scale electrochemical-mechanical model and studied the radial stress and eigen-strain developed in the electrode during discharge. However, the present model focuses on exploring the electrochemical and thermal responses to a mechanical failure induced short circuit. For simplicity, we consider the internal stresses from diffusion negligible. To accurately model an electrical short, it is important to predict explicitly the mechanical failure behavior of the individual layers including the fracture area/shape and modes (see reference (21) for a detailed description of Mode I, Mode II and Mode III) corresponding to the short area and short resistance, respectively. A generic strain based failure criterion can be written as:

$$f(\varepsilon_{ij}) = 1 \tag{17}$$

Using the mechanical model presented in the previous section, we can predict the mechanical failure of an individual layer (e.g., the separator), which will then initiate a change in the short circuit resistance. One representation of the short resistance calculation is written as follows:

$$R_{short} = A_{short} \sum \frac{1}{K_s^i} \tag{18}$$

$$A_{short} = \sum_{i=1}^{n} A_i \tag{19}$$

where R_{short} is the electrical short resistance with units of Ω-m^3, A_{short} indicates the area of short circuit and A_i is the surface area of each element, K_s^i is the electrical conductivity for all components involved in the short circuit. For example, before short circuit, the electrical path involves an anode, a separator and a cathode, in that order; while the loop consists only of the anode and cathode layers after a short circuit induced by tensile failure of the separator. Knowing the short-circuit resistance, we will then be able to update the discharge current (i_{app}) in Eq. [14] of the electrochemical model.

We note that the explicit solver of LS-DYNA is utilized to solve the mechanical model, which generally has a scaled loading time (0.01 ~ 1 s) and a very small time step (1e-6 ~ 1e-9 s). However, for an actual quasi-static test, the loading time can be hundreds seconds. So when communicating fluxes and source terms between the meso-scale mechanical model and electrochemical-thermal model, the time and time steps for the battery model are scaled accordingly, based on the ratio of the numerical loading rate and the experimental loading rate.

Results and Discussion

To verify the model developed above, a single element benchmark study is conducted. We start with a numerical verification of the macro-meso mechanical homogenization method, followed by a preliminary case study for a short-circuit induced by compression of the cell. We also present a parametric study on the effect of short

resistance. The thickness of the macro element, anode, separator and cathode are 180 µm, 85 µm, 25 µm and 70 µm, respectively. The in-plane size of the element is 0.5 mm.

Verification of Mechanical Homogenization Model

As a preliminary study, a linear elastic case is presented considering the electrodes and separators all exhibit isotropic elasticity. We assume that the cathode and anode both have a Young's modulus of 40 GPa, and that the Young's modulus of separator is 4 GPa. The Poisson's ratios of all components are set to 0.3. Two loading conditions, in-plane tension and through-thickness compression, are studied using the macro-meso model (named as the Multiscale Model) that has only one element and compared with the actual model with multiple layers (named as Multilayer Model) that has three elements each representing one of the components. The strain and stress profiles are plotted and compared, as shown in Figure 3. As seen from the results, the multiscale model predicts the stress/strain responses accurately for the in-plane tensile loading condition, which has been known to be the primary failure condition of separator layer (7). For the through-thickness compression case, some discrepancy of the predicted stress/strain has been observed with errors less than 18%. The error is attributed to the assumptions underlying Eqs. [6-9], that we employed in this approach. Overall, the multiscale model exhibits acceptable accuracy in predicting the mechanical deformation of the battery cell and cell components.

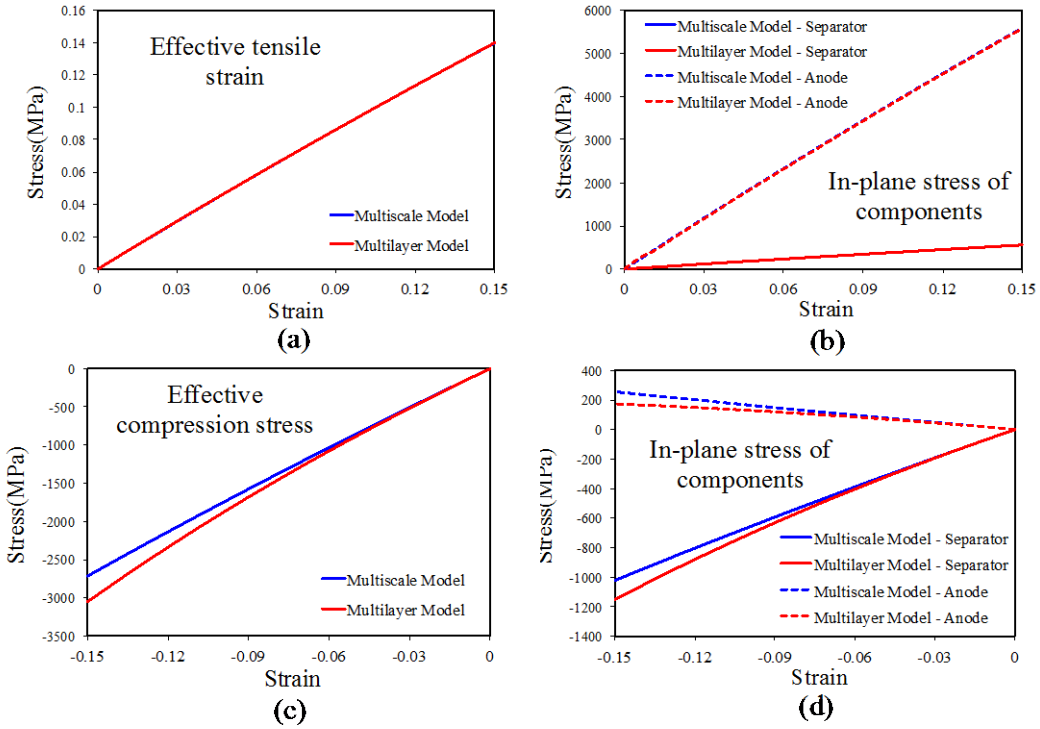

Figure 3. Comparison of numerical results for multiscale model and multilayer model: (a) effective in-plane tensile strain under in-plane tension, (b) in-plane stress of separator and anode under in-plane tension, (c) effective through-thickness compression stress under through-thickness compression and (d) in-plane stress of separator and anode under though-thickness compression.

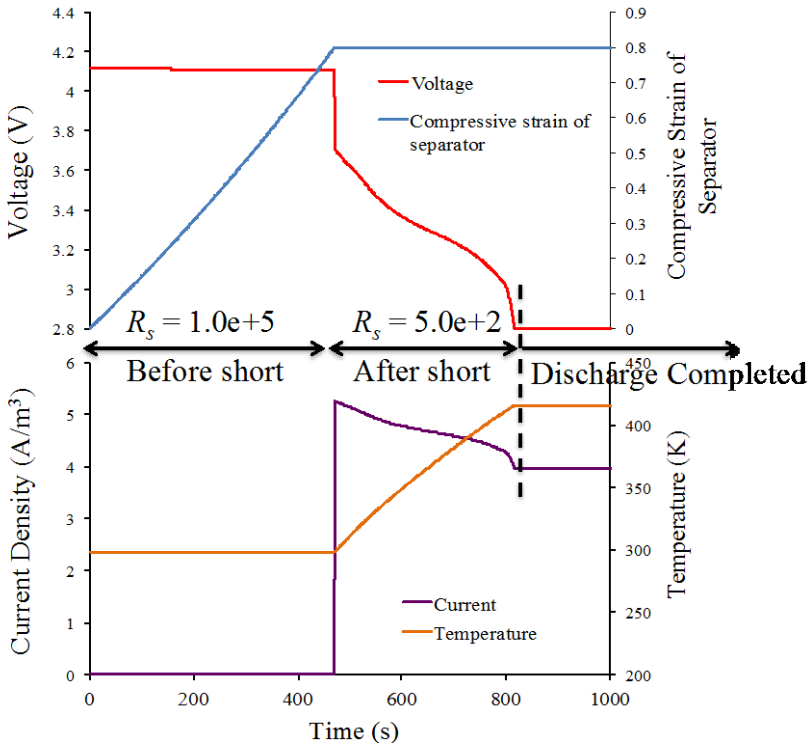

Figure 4. Voltage, current density and temperature profiles versus strain profile of the separator during a compressive load.

We also note that the current multiscale model provides a generic framework for studying the mechanical and coupled mechanical-electrochemical-thermal responses. The individual pieces of the model, e.g., the mechanical homogenization approach, electrochemical model and correlation of short resistance can be further enhanced using more sophisticated models, when available.

Prediction of Short-Circuit Responses

For a uniform through-thickness compression of the element, we assign a failure compressive strain of 0.8 for the separator layer. A constant loading rate of 0.00015 mm/s is applied and the displacement holds following by the failure of separator layer. Figure 4 shows the voltage, current density and temperature profiles against the strain history of the separator layer. The parameters of the battery model correspond to that of an 800 mAh $LiCoO_2$/graphite cell. As we can see, during the initial stage before the short circuit, there is a slight decrease in the cell voltage from 4.113 V to 4.107 V. Followed by the failure of separator, an instantaneous drop of voltage is observed due to the sudden increase in the current density from 0.012 A/m^3 to 5.26 A/m^3. We note that the instantaneous drop of voltage was not captured in our previous coupled mechanical-electrical-thermal model (17). Subsequent gradual decrease of cell voltage and levelling off of the current density are consistent with the experimental observations during mechanical abuse tests (22). On the other hand, the temperature increases continuously after the short due to the increasing contributions from the Joule heating energy and the electrochemical reaction energy. The internal resistances for the cell prevent any further discharge below 2.8V for the parameter set chosen for the electrochemical model. Also, since we assumed adiabatic boundary conditions, there is no thermal conduction of the heat away from the single element and so the temperature remains constant after

complete discharge. The previous model we presented (17) considered only the mechanical-electrical-thermal effects, neglecting contributions from the electrochemical reactions. The current model simulates more accurately the short-circuit behavior due to the introduction of electrochemical reactions and the energy conservation equation for the battery's reaction heats.

Effect of Short Circuit Resistance

The short resistance is of great importance for the prediction of short-circuit behavior. The characterization of short resistance is very challenging due to its sensitivity to parameters not readily measurable, like contact area, shape of short area and contact pressure etc. Numerically, it can be estimated in the model presented above using Eq. [18] provided above. Alternately, to accurately capture the experimental trends, this parameter can be regressed from data. Regardless, the capability to capture the effect of short resistance is an important measure of an abuse-response model. To study the effect of short resistance, specific values of short resistance are assigned (R_s = 50, 100 and 500) this section. Figure 5 compares the current density and voltage profiles for the short circuit with different values for the short circuit resistance. As seen from the results of Fig. 5, a lower resistance corresponds to a higher instantaneous increase of current and drop of voltage. This will then results in a quicker fully discharging of the cell. The total heat generation depends on both the magnitude of current/voltage and also their duration. The temperature profiles for different short resistances are compared in Figure 6, where we can see a relatively higher temperature for resistance decreasing from 500 Ωm^3 to 100 Ωm^3 and a decreasing of temperature as the short resistance further decreases from 100 Ωm^3 to 50 Ωm^3. The trade-off between the short-circuit resistance and the thermal runaway response was previously discussed in (24) where such trends were attributed to a trade-off between total heat generated and the heat generation rate. Such complicated behavior further highlights the need for accurate characterization of short resistance values and drives the development of advanced modeling techniques.

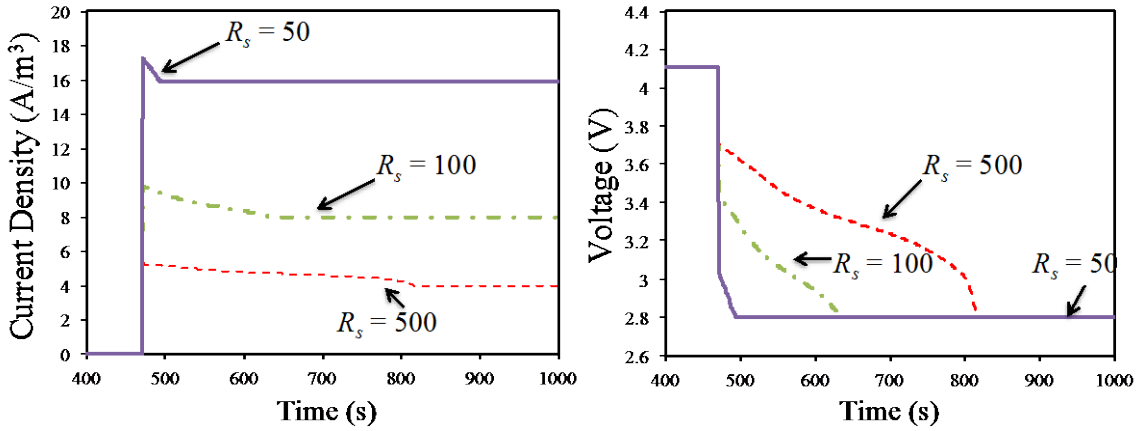

Figure 5. Effect of short resistance on the current density and voltage profiles

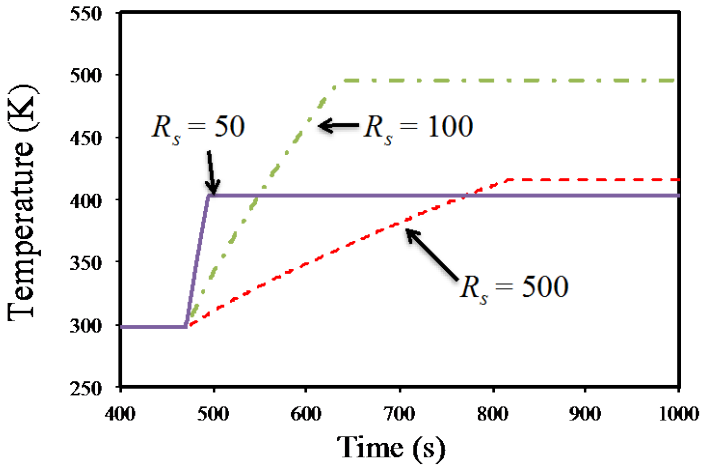

Figure 6. Effect of short resistance on the temperature profile

Conclusion

We presented a multiscale simultaneously coupled mechanical-electrochemical-thermal modeling framework, which was implemented in commercial software LS-DYNA as a user-defined material model. The multiscale mechanical model enables a combination of computational efficiency and accurate modeling of failure location. The mechanical model is coupled with the electrochemical-thermal model at microscale through exchange of variables like displacement and temperature. A single element numerical verification study is presented. From the preliminary numerical results, we verify the accuracy of the multiscale mechanical model, and demonstrate the capability of the model to predict mechanical abuse induced short-circuit behavior and the effect of short resistance. To extend the current model to a full cell simulation, we need to address continuity and boundary equations for the electrochemical model which will be presented in a future work.

Acknowledgments

This study was supported by Computer Aided Battery Engineering Consortium (CAEBAT) project of the Vehicle Technologies Office, Office of Energy Efficiency and Renewable Energy, U.S. Department of Energy under contact number WBS1.1.2.406. The research was performed using computational resources sponsored by the Department of Energy's Office of Energy Efficiency and Renewable Energy, located at the National Renewable Energy Laboratory.

References

1. T. Wierzbicki and E. Sahraei, *J. Power Sources*, **241**, 467 (2013).
2. E. Sahraei, J. Meier and T. Wierzbicki, *J. Power Sources*, **247**, 503 (2014).
3. E. Sahraei, J. Campbell and T. Wierzbicki, *J. Power Sources*, **220**, 360 (2012).
4. E. Sahraei, M. Kahn and J. Meier et al., *RSC Advances*, **5**(98), 80369 (2015).
5. E. Sahraei, R. Hill and T. Wierzbicki, *J. Power Sources*, **220**, 360 (2012).
6. W. J. Lai, M. Y. Ali and J. Pan, *J. Power Sources*, **245**, 609 (2014).
7. W. J. Lai, M. Y. Ali and J. Pan, *J. Power Sources*, **248**, 789 (2014).
8. M. Y. Ali, W. J. Lai and J. Pan, *J. Power Sources*, **242**, 325 (2013).

9. M. Y. Ali, W. J. Lai and J. Pan, *J. Power Sources*, **273**, 448 (2015).
10. J. Xu, B. Liu and X. Wang et al., *Appl. Energy*, **172**, 180 (2016).
11. J. Xu, B. Liu and D. Hu, *Sci. Rep*, **6**, 21829 (2016).
12. J. Xu, B. Liu and L. Wang et al., *Eng. Fail. Anal.*, **53**, 97 (2015).
13. J. Xu, L. Wang and J. Guan et al., *Mater. Design*, **172**, 180 (2016).
14. S. Pannala, J. A. Turner and S. Allu et al., *J. Appl. Phy.*, **118**(7), 072017 (2015).
15. H. Wang, S. Simunovic and S. Maleki et al., *J. Power Sources*, **306**, 424 (2016).
16. C. Zhang, S. Santhanagopalan and M. Sprague et al., *J. Power Sources*, **290**, 102 (2015).
17. C. Zhang, S. Santhanagopalan and M. Sprague et al., *J. Power Sources*, **298**, 309 (2015).
18. C. Zhang, N. Waksmanski and V. M. Wheeler, *I. J. Eng. Sci.*, **94**, 1 (2015).
19. M. B. Effat, C. Wu and F. Ciucci, *Asia-Pac. J. Chem. Eng.*, **11**(3), 399 (2016).
20. S. Golmon, K. Maute and M. L. Dunn. *Comput. Strut.,* **87**(23), 1567 (2009).
21. M. F. Kanninen and C. L. Popelar, *Advanced fracture mechanics*, Oxford University Press, Oxford (1985).
22. P. Ramadass, W. Fang and Z. Zhang, *J. Power Sources*, **248**, 769 (2014).
23. M. Guo and R.E. White, *J. Electrochem. Soc.*, **158**(10), A1166-A1176 (2011).
24. S. Santhanagopalan, P. Ramadass and Z. Zhang, *J. Power Sources*, **194**(1), 550 (2009).